IAC-24-A1.2.3

On the various numerical methods for the high-fidelity simulation of thermovibrationally-driven solid particle accumulation phenomena in microgravity conditions

Balagopal Manayil Santhosh[a] , Ali Anwar and Marcello Lappa[a*]

[a] *Department of Mechanical and Aerospace Engineering, University of Strathclyde, James Weir Building, 75 Montrose Street, Glasgow, G1 1XJ, UK*
* Corresponding Author (Marcello.lappa@strath.ac.uk)

Abstract

New microgravity-based contactless solid particle manipulation strategies relying on the application of thermal stimuli to a fluid in combination with imposed high-frequency vibrations offer promising directions for the production in space of new materials that cannot be obtained in normal gravity conditions. This line of inquiry, originating from a theory formulated ten years ago, has recently received confirmation by virtue of experiments conducted on board the ISS using the Selectable Optical Diagnostic Instrument (SODI) in conjunction with the Microgravity Science Glovebox (MSG). These experiments have also revealed interesting effects, which were not included in the original theory and need now to be properly interpreted, understood and modeled. In such a context, this study is devoted to a critical comparison of different available Eulerian-Lagrangian numerical strategies potentially able to reproduce the experimental findings and reveal in detail the underlying mechanisms. These differ in regard to the degree of fidelity with which the interactions between the suspended solid particles and the carrier fluid are implemented. Different numerical approaches with increasing complexity are used as the discussion progresses. Starting from the simplest possible case where the back influence of particles on fluid flow is disregarded (one-way coupling), we then consider the standard two-way coupling model by which the liquid and solid phases are fully coupled in terms of momentum exchange and the Dense Discrete Particle Modelling (DDPM) where in addition to the localized exchange of momentum, the inter-particles stresses are also somehow taken into account by analogy with the kinetic theory of gases. Finally, a four-way coupling strategy is implemented, where effective particle collisions are also simulated (through proper coupling of Ansys Fluent and Rocky software). We show that different approaches display a varying degree of success in reproducing properly the experiments, which depends on the ability of the solver to capture properly particle inter-stresses.

Keywords: Solid particle dynamics, Thermovibrational flow, attractors, Particle structures, Numerical simulation

Nomenclature

α	*Fluid thermal diffusivity*
β_T	*Fluid thermal expansion coefficient*
ω	*Angular frequency*
ρ	*Fluid density*
$g(t)$	*Time varying acceleration*
b	*Amplitude(m)*
f	*Frequency in hertz*
L	*Characteristic length*
γ	*Non-dimensional acceleration amplitude*
ξ	*Particle to fluid density ratio*
Ω	*Non-dimensional angular frequency*
Pr	*Prandtl number*
t	*Non-dimensional time*
μ	*Dynamic viscosity*
Ra_ω	*Vibrational Rayleigh number*
St	*Particle Stokes number*

Acronyms/Abbreviations

Computational Fluid Dynamics- Discrete Element Method (CFD-DEM)
Commercial Resupply Service mission 26 (CRS)
Discrete Phase Model (DPM)
Dense Discrete Phase Model (DDPM)
Discrete Element Method (DEM)
European Space Agency (ESA)
Experiment Scientific Requirements (ESR)
International Space Station (ISS)
Kinetic Theory of Granular Flows (KTGF)
Microgravity Science Glovebox (MSG)
National Aeronautics and Space Administration (NASA)
Payload Integration Agreement (PIA)
Selectable Optical Diagnostic Instrument (SODI)
Science and Technology Facilities Council (STFC)
Thermovibrationally-driven Particle self-Assembly and Ordering in Low Gravity (T-PAOLA)
The United Kingdom Research and Innovation (UKRI)
The United Kingdom Space Agency (UKSA)

1. Introduction

The techniques of self-assembly and induced particle clustering are swiftly emerging as key strategies for building diverse systems that incorporate various types of components at both the nano and micro levels. These methods are transforming the design of intricate, multi-functional structures by allowing different elements to organize themselves into well-ordered configurations spontaneously, eliminating the need for significant external intervention. Mastering the creation of materials and systems at such scales opens up vast potential across numerous disciplines, including materials science, biotechnology, and nanotechnology.

In such a context, this study builds on a well-established research initiative that has received continuous support over the past five years through multiple grants from UKRI, with additional financial and technical backing from the UK Space Agency, the European Space Agency (ESA), and NASA under international collaborations. The programme, titled Thermovibrationally-driven Particle self-Assembly and Ordering in Low Gravity (PI: M. Lappa, referred to by the UK Space Agency as "T-PAOLA" and by NASA/ESA as "PARTICLE VIBRATION"), was initially designed to investigate an innovative method for the non-contact manipulation of solid particles suspended in a fluid under microgravity conditions. This method leverages the effects of "vibrations" and "differential heating" to control particle behavior.

This line of research, which traces its origins back to a theoretical framework developed a decade ago, led to the identification of a novel class of solid particle “attractors” within liquids. These attractors are specific regions within a fluid container where particles naturally gather and form highly organized patterns of various shapes and sizes. The structures formed are influenced by the frequency, amplitude, and direction of the vibrations applied, as well as the intensity of the temperature gradient imposed [1-8]. The scientific and technological significance of this finding is substantial. Many liquid materials—whether inorganic or organic—are composed of small particles or droplets (a "minority phase") dispersed within a fluid matrix [9], and the eventual properties of these materials in their solid state are greatly influenced by how this minority phase is distributed spatially [10-14].

While magnetic fields offer one way to manipulate such particles without contact, their application is limited to electrically conductive or responsive materials. Vibrations, on the other hand, provide a more versatile solution, as they can be applied to a much broader range of fluids and particles without the need for electrically conductive substances [15-16]. Moreover, since this technique does not rely on forces between particles to achieve ordered structures, it is suitable for systems where particles are sparse or lack any natural tendency to cluster or move autonomously. Looking ahead, this novel approach to particle manipulation in microgravity has the potential to lead to the creation of new materials—both inorganic and organic—with unique properties that cannot be replicated in Earth’s gravity [17].

1.1 Historical Details

The PARTICLE VIBRATION (T-PAOLA) project was initially chosen by the UK Space Agency (UKSA) and the Science and Technology Facilities Council (STFC) as part of the 2018 UKSA Announcement of Opportunity for UK Microgravity Experiments. The selection followed a highly competitive peer-review process. The project was specifically designed to capitalize on the unique capabilities of NASA’s Microgravity Science Glovebox (MSG) facility (illustrated in Fig. 1, left), used in conjunction with the Selectable Optical Diagnostic Instrument (SODI), an ESA payload. SODI’s modular design includes a subsystem for generating controlled vibrations [18], some of which are visible in the left panel of Fig. 1. The combined use of these two resources was made possible through a Payload Integration Agreement (PIA) between NASA and ESA, later expanded to include the UK Space Agency for this specific project. Additional specialized hardware to accommodate the fluid-particle mixtures central to the experiments was produced in the United Kingdom by QinetiQ [18].

This research project is rooted in a theory developed nearly a decade ago [2], which predicted that the combination of particle "inertial" effects (caused by differences in particle density relative to the surrounding fluid) and "thermovibrational" effects (fluid movement triggered by the simultaneous application of temperature gradients and vibrations) could lead to particle self-organization. Over time, this theoretical framework has been expanded and refined through a series of detailed studies that relied on complex mathematical models and numerical simulations [3-8, 17]. These investigations helped define the specific parameters for space-based experiments, which were compiled into the ESR (Experiment Scientific Requirements) document. This document guided the design of the necessary hardware and the selection of experimental materials.

Several tests and activities have been carried out over the past five years to validate the space-bound hardware and streamline various procedures. For example, long-term compatibility tests [18] were conducted from December 11, 2019, to June 11, 2020, to ensure the compatibility of the selected liquid (ethanol) and particles (glass and silver) with the materials used to construct the hardware. Manufacturing

of the experimental cell arrays, which included quartz fluid containers and heating elements, began in April 2019 and concluded on July 18, 2020. These cell arrays then underwent thermal acceptance tests in September 2020 to confirm their resilience under the temperature conditions expected during launch and in space aboard the International Space Station (ISS). Between October and December 2020, the procedures for injecting liquids and particles with varying densities into the fluid containers were tested and optimized to minimize particle damage during injection [18]. Additionally, in February 2021, tests were conducted to verify that the glass particles could endure the typical launch vibrations generated by the SpaceX Falcon rocket [18].

The Mission Operation Implementation Concept (MOIC) document, detailing the necessary steps for conducting the experiments in space, was finalized on April 28, 2022. In June 2022, the fluid containers were filled with the required degassed liquids and particles at a facility in Farnborough. Further functional tests to verify the performance of the thermal control system and temperature sensors were carried out between June and July 2022. A joint Final Acceptance Review (FAR) by ESA and UKSA took place during the summer of 2022, after which the UK Space Agency signed the Certificate of Conformity/Acceptance on October 12, 2022.

1.2 Current Project Status

On November 26, 2022, at 7:20 PM UK time, NASA and SpaceX successfully launched the SpaceX Falcon rocket, which stands 70 meters tall, from Kennedy Space Center's Launch Pad 39A. The rocket carried the hardware for the PARTICLE VIBRATION experiment. The next day, November 27, 2022, at 12:20 PM UK time (7:39 AM EST), the CRS-26 SpaceX Dragon cargo spacecraft (Fig. 1, right) autonomously docked with the space-facing port of the ISS's Harmony module.

On February 3, 2023, astronaut Frank Rubio completed the installation of the PARTICLE VIBRATION hardware in the Microgravity Science Glovebox (MSG) without any complications (Fig. 1, left). Following the installation, on February 9, 2023, the Principal Investigator (PI) remotely commanded the optical checkout activities from the ground. These tasks were critical for fine-tuning the optical parameters, such as exposure time, gain, and black level, needed for laser-based visualization of the particles.

After the hardware installation and successful completion of the functional and optical checkouts, more than 160 experiments were conducted between February and April 2023. These experiments systematically varied parameters such as the temperature gradient applied, the frequency and amplitude of the vibrations, and involved testing four different types of particles. While all particles were made of glass and silver, they varied in size and density [18].

Fig. 1 - Astronaut Frank Rubio installing the PARTICLE VIBRATION Hardware into the Microgravity Science Glovebox (MSG) on board the ISS (3rd Feb 2023).

Throughout the project, telemetry data (including temperature records) and representative images from the SODI hardware's interferometers, showing the progression of the vibrating particles at selected intervals, were transferred from the ISS to the Principal Investigator located in the UK. This was facilitated by a sophisticated infrastructure, including NASA's Marshall Space Flight Center in Huntsville, Alabama (also known as the Huntsville Operations Support Center, HOSC), and the European User Support and Operations Centre (E-USOC) in Madrid, Spain, which is part of ESA's support network.

The experiments have provided substantial confirmation of the thermovibrational-inertial theory originally developed by the Principal Investigator in 2014 and further refined over the years [1-8]. These preliminary findings have emerged from the daily transmission of images and telemetry data from the ISS, which represents only a small portion of the vast amount of data stored onboard in dedicated hard drives. Initial visual inspection of these fringe images (e.g., Fig. 2) has confirmed the capacity of the thermovibrational-inertial effect to induce particle self-assembly and the formation of distinct structures. These formations occur within specific ranges of temperature differences and vibration parameters (frequency and amplitude). As predicted, the location and organization of these structures are influenced by particle density and size.

The present study describes current activities at the University of Strathclyde being implemented to improve the agreement between experimental findings and numerical simulations. The goal is to gain deeper

insight into the mechanisms governing particle behavior in fluid flow. The new models include the effects of inter-particle stresses, a feature absent from the earlier two-way coupled model, which only accounted for momentum transfer between the fluid and particles but did not consider the additional stresses resulting from particle-particle interactions. Although those models were extensively used to plan and optimize the experiments in space, new levels of sophistication are needed to capture more precisely the physics at work in those experiments and explain some discrepancies.

2. Mathematical models

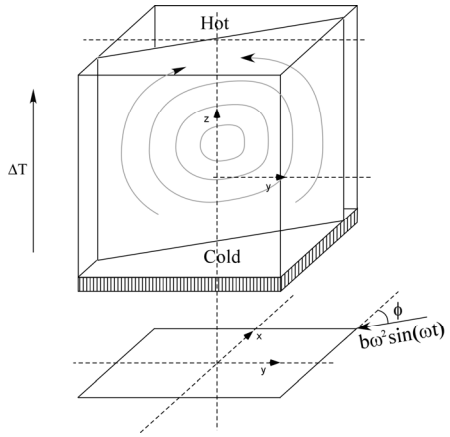

Fig. 2 - Cubic cavity with characteristic size L, delimited by solid walls (one at z=-0.5 cooled, the other at z=0.5 heated, adiabatic conditions on the remaining sidewalls). In this study, the vibrations are parallel to the y axis.

2.1 Geometric model

The considered geometric model simply reflects the effective experimental configuration [18], namely a differentially heated cubic enclosure undergoing vibrations along a direction perpendicular to the imposed temperature difference (as shown in Fig. 2, temperature difference and vibrations are along the z and y axes, respectively, while x plays the role of 'spanwise direction'). The imposed vibrations are modelled via a simple sinusoidal function, i.e. as $b\omega^2 \sin(\omega t)\ \underline{\hat{n}}$ where b (m) and $\omega=2\pi f$ and (rad/s) are the vibration amplitude and angular frequency, respectively (f being the frequency in hertz) and $\underline{\hat{n}}$ is the unit vector associated with the shaking direction.

2.2 Hybrid Eulerian-Lagrangian formulation

Building on the success of previous studies [2-7], this work adopts a hybrid approach. In this method, fluid motion is analyzed using a Eulerian framework, which results in the traditional Navier-Stokes equations applicable to a continuous medium. Meanwhile, particle transport is addressed through a Lagrangian perspective, allowing each particle to be treated as an individual element that interacts with its surroundings..

The fluid phase is obviously governed by the classical Navier-Stokes equations, which, for an incompressible fluid, can be cast in condensed form as

$$\underline{\nabla}\cdot\underline{V}=0 \tag{1}$$

$$\rho\frac{\partial \underline{V}}{\partial t}=-\underline{\nabla}p-\rho\underline{\nabla}\cdot\left[\underline{V}\underline{V}\right]+\mu\nabla^2\underline{V}+\rho b\ \omega^2\sin(\omega\ \mathrm{t})\underline{\hat{n}}+\underline{S}_m \tag{2}$$

$$\rho C_v\frac{\partial T}{\partial t}+\rho C_v\underline{\nabla}\cdot\left[\underline{V}T\right]=\lambda\nabla^2 T \tag{3}$$

where the vector $\underline{V}$ contains the variables $[u, v, w]$ (u, v and w being its velocity components along the x, y and z directions), p is the pressure, T is the temperature and ρ, μ, λ and C_v are the fluid density, dynamic viscosity, thermal conductivity and specific heat at constant volume, respectively. The contribution $\rho b\ \omega^2\sin(\omega\ \mathrm{t})\underline{\hat{n}}$ accounts for the buoyancy force produced by the imposed vibrations in the framework of the so-called Boussinesq approximation. Moreover, the additional vector quantity $\underline{S}_\mathrm{m}$ at the right-hand side of eq. (3) is the term required to properly couple the liquid and solid phases.

Microscopic quantities, such as individual particles, are clearly distinct and isolated when compared to field variables. However, the forces typically acting upon these particles and their resulting motion can be effectively analyzed through the Maxey-Riley equation. A brief summary of this equation is provided below, with a more in-depth exploration available in the work of Maxey and Riley [19]. In its vector form, the equation is expressed as:

$$\begin{aligned}\rho_p\frac{d\underline{V}_p}{dt}&=\rho\frac{D\underline{V}}{Dt}+\frac{9}{2}f(\mathrm{Re}_p)\frac{\mu}{R_p^2}\left(\underline{V}-\underline{V}_p\right)+\\&\frac{\rho}{2}\left(\frac{D\underline{V}}{Dt}-\frac{d\underline{V}_p}{dt}\right)+\left(\rho_p-\rho\right)\mathrm{b}\ \omega^2\sin(\omega\ \mathrm{t})\underline{\hat{n}}+\underline{S}_{ParticlInt}\end{aligned} \tag{4}$$

where ρ_p is the particle density, $\underline{V}_\mathrm{p}=[u_\mathrm{p}, v_\mathrm{p}, w_\mathrm{p}]$ is the particle velocity and Re_p is the related instantaneous Reynolds number, defined as

$$\mathrm{Re}_p=\frac{2R_p\rho\left|\underline{V}-\underline{V}_p\right|}{\mu} \tag{5}$$

f(Rep) is a corrective factor required (where R_p is the particle radius) to account for the departure of the drag from the classical Stokes law:

$$f\left(\mathrm{Re}_p\right) = 1 + 0.15\,\mathrm{Re}_p^{\,0.687} \tag{6}$$

When organized in this manner, equation (4) can be interpreted as a balance of forces. The five terms on the right-hand side represent various contributions: the force on the particle from the undisturbed flow, the drag, the virtual added mass force, the time-dependent buoyancy force due to vibrations, and the additional force caused by particle interactions ($\underline{S}_{partclInt}$). The Basset force is omitted, as the flow frequencies under consideration fall within a range where neglecting it is permissible (see [20] and relevant literature for a comprehensive discussion, which is excluded here for brevity). The velocity of the liquid, $\underline{V}$, appearing in this equation is determined at each particle's location by reconstructing it from nearby grid points. To ensure accurate results, this requires the application of an appropriate interpolation scheme [2-7].

2.3 Coupling Level

Various levels of coupling are possible according to the assumptions made and models assumed for the two specific source terms $\underline{S}_m$ and $\underline{S}_{PartclInt}$ appearing in eqs. (2) amd (4), respectively.

2.3.1 One-way coupling

In this case, the following basic assumptions are made:

$$\underline{S}_m = 0 \tag{7}$$

$$\underline{S}_{PartclInt} = 0 \tag{8}$$

Put simply, eq. (7) implies that while the motion of solid particles is influenced by the fluid flow, particles are not able to influence the carrier fluid. In this case, the number of particles used for the simulation has no impact on the observed fluid flow dynamics, which depend only on the presence of external forces (the periodic acceleration induced by vibrations in this case and the ensuing buoyant effects). In turn, particle dynamics depend on the ability of the velocity field to support the existence of particle "attractors", i.e. loci of space where particles tend to naturally cluster as time passes, and on particle *inertial properties* (particles having a finite mass and size that cause a departure of their trajectories from the streamlines of the carrier flow). As the $\underline{S}_{PartclInt}$ is also set to zero, particle interactions play no role, which means the number of particles used for the simulations has no impact on particle dynamics either (a relatively large number of particles being typically used in the simulation only to reveal the perfection of the underlying "attractors").

2.3.2 Two-way coupling

In this model, return effects are adequately addressed through the inclusion of the interphase coupling terms,
S, in equation (2). To ensure the overall approach remains physically coherent, this term must be calculated for each control volume. Consequently, an algorithm is required to identify the particles present within any computational cell at a given time. Formally, if we denote the number of particles in a cell as n_{ijk} (i, j and k being the representative indexes of the x, y and z directions, respectively), the interphase term can be expressed (see, e.g., [21,22,8]) for each computational cell as

$$\left(\underline{S}_m\right)_{ijk} = -\frac{1}{\delta\Omega_{fluid}} \sum_{\ell=1}^{n_{ijk}} m_{p\ell} \frac{d\underline{V}_{p\ell}}{dt} \tag{9}$$

$$\delta\Omega_{fluid} = \delta\Omega_{ijk} - n_{ijk} \frac{4}{3}\pi R_p^3 \tag{10}$$

Where, as explained before, R_p is the particle radius. The negative sign preceding the summation indicates that when particles are accelerating (i.e., $dV_p/dt>0$), the thermovibrational flow experiences a corresponding deceleration ($\partial V/\partial t<0$), and vice versa. In this expression, m_p and $\delta\Omega_{ijk}$ represent the mass of an individual particle and the volume of the computational cell that contains it, respectively, denoted by

$$m_p = \rho_p \frac{4}{3}\pi R_p^3 \quad , \quad \delta\Omega_{ijk} = \Delta x \Delta y \Delta z \quad . \tag{11}$$

Additionally, $\delta\Omega_{fluid}$ refers to the amount of fluid within the computational cell. By basic geometric reasoning, this value can be formally determined by subtracting the volume occupied by all particles in the cell from $\delta\Omega_{ijk}$.
Like the one-way coupling, with this approach, typically, the inter-particle force term appearing in eq. (4) is neglected, i.e. $\underline{S}_{PartclInt}$ =0. Although, particles cannot influence each other, however, their overall number (or concentration) does play a role in determining the emerging dynamics as momentum can be transferred back from particles to the surrounding fluid.

2.3.3 Dense Discrete Phase Model (DDPM)

The so-called Dense Discrete Phase Model (DDPM) brings in an additional degree of sophistication by modifying the fluid governing equations by taking into account the fluid volume fraction φ

$$\rho\frac{\partial\varphi}{\partial t}+\rho\underline{\nabla}\cdot\left[\varphi\underline{V}\right]=0 \tag{12}$$

$$\rho\frac{\partial\left(\varphi\underline{V}\right)}{\partial t}=-\varphi\underline{\nabla}p-\rho\underline{\nabla}\cdot\left[\varphi\underline{V}\underline{V}\right]+\underline{\nabla}\cdot\left[\mu\varphi(\underline{\nabla V}+\underline{\nabla V}^{T})\right]$$
$$+\rho\varphi b\ \omega^{2}\sin(\omega\ t)\underline{\hat{n}}+\underline{S}_{m} \tag{13}$$

Moreover, an algorithm is put in place to prevent particles from undergoing unphysical concentration in the same portion of space (no particle interpenetration is allowed) and an “ensemble model” is introduced to determine the particle-to-particle force term, i.e. it should be seen as an approach by which the additional forces resulting from particle interactions need not to be modelled explicitly but are somehow accounted for by means of a statistical paradigm.

In other words, instead of directly simulating particle collisions and uncorrelated movements, which would be computationally prohibitive, these interactions are represented using the kinetic theory of granular flows (KTGF). As a result, the governing equations remain the same as those outlined in Sect. 2.3.2, with the exception of the source term of (4) [23,24], which reads:

$$\underline{S}_{PartclInt}=-\frac{1}{\rho_{p}\varphi_{p}}\underline{\nabla}\cdot\underline{\underline{\tau}}_{p} \tag{14}$$

where φ_p is the local particle volume fraction (determined by using the particle data obtained through solution of the corresponding Lagrangian particle tracking equation, i.e. (4)):

$$\varphi_{p}=\frac{n_{ijk}\frac{4}{3}\pi R_{p}^{3}}{\delta\Omega_{ijk}} \tag{15}$$

which also serves to determine the corresponding fluid volume fraction (appearing in eq. (12) as φ=1-φ_p. Moreover, $\underline{\underline{\tau}}_{p}$ is the so-called solids or particle stress tensor, which in turn consists of the particles-induced normal and shear viscous stresses as well as the normal pressure:

$$\underline{\underline{\tau}}_{p}=-p_{p}\underline{\underline{I}}+2\mu_{p}\left(\frac{\underline{\nabla\tilde{V}}_{p}+\underline{\nabla\tilde{V}}_{p}^{T}}{2}\right)+\left(\lambda_{p}-\frac{2}{3}\mu_{p}\right)\underline{\nabla}\cdot(\underline{\tilde{V}}_{p}\underline{\underline{I}}) \tag{16}$$

In this equation, $\underline{\tilde{V}}_{p}$ represents the average velocity vector of the solid phase, p_p, μ_p and λ_p are the solid pressure, particle phase viscosity, and bulk solid viscosity, respectively, which are derived from KTGF principles. These values are determined based on the conservation of the kinetic energy associated with uncorrelated particle motions, a concept introduced by Lun et al. [25]. This energy is commonly referred to as "granular temperature," a term adapted from kinetic gas theory, where temperature quantifies the energy within the random motion of molecules. The granular temperature is monitored through the solution of an additional transport equation (which is not included here for brevity). For further information, interested readers are directed to [24,26]. Here we limit ourselves to mentioning that, as both the granular temperature equation and eq. (16) are solved with the averaged particle velocity $\underline{\tilde{V}}_{p}$, in general, a sufficient statistical representation of the particle phase is needed to ensure a stable behavior of such equations.

2.3.4 Four-Way Coupling: Discrete Element Method (DEM)

With the Discrete Element Method (DEM), the degree of fidelity of the algorithm, i.e. its ability to reproduce the physics at play in granular systems, is further improved by modelling in detail particle interactions on the basis of binary interference/collision models.

The DEM generally calculates the interaction force for each spherical particle as the combination of two distinct contributions, one of elastic-plastic nature ($\underline{F}_{ij}^{n}$) and another one ($\underline{F}_{ij}^{t}$) essentially related to frictional effects:

$$\underline{S}_{PartclInt}=\underline{F}_{ij}^{n}+\underline{F}_{ij}^{t} \tag{17}$$

To accurately describe these forces, it is essential to differentiate between the hard-sphere and soft-sphere models. In the hard-sphere model, particles are treated as rigid, disallowing deformation or overlap, and the forces between them are modeled as instantaneous, or "impulsive" [27]. In contrast, the soft-sphere model employed by the DEM allows some overlap between particles, although they remain undeformable [28]. This overlap enables a more straightforward calculation of the normal force, which depends on the degree of overlap [29]. The Discrete Element Method (DEM) uses virtual springs perpendicular to the contact plane, based on the Hertzian Model from the 19th century. In this model, the normal force is both repulsive and includes a damping term for dissipative effects. Walton and Braun [30] extended this approach by considering hysteretic effects—irreversible energy loss during loading and unloading. Instead of using complex elastic-damping springs, they proposed a simpler linear model where different slopes are applied for loading and unloading phases, reflecting the plastic behavior of materials

during particle interactions. This model thus captures the asymmetry in force response more efficiently (see Fig. 3).

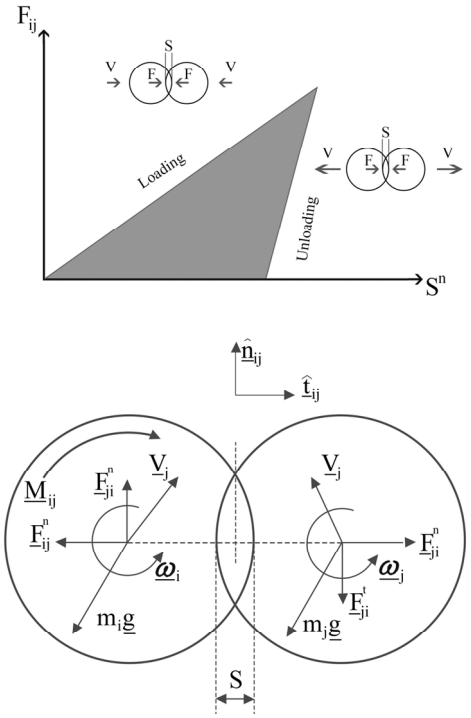

Fig. 3 - (a) Sketch of interacting particles and related kinematic and dynamic quantities; (b) particle loading-unloading

As shown in the figure, while the slope of the linear loading branch K_l^n is moderate, the slope of the unloading branch K_u^n is notably steeper. This results in a "residual displacement" (S_o) when the normal force drops to zero during the unloading phase (Walton [31]; see Fig. 3). In terms of algorithm implementation, Rocky software (used in this study) applies this model in the following way [32-34]:

$$\underline{F}_{ij}^{n,(\tau)} = \begin{cases} \min\left(\underline{F}_{ij}^{n,(\tau-\Delta\tau)} + K_u^n \underline{\Delta S}^n,\ K_l^n \underline{S}^{n,(\tau)}\right) & if\ \Delta S^n \geq 0 \\ \max\left(\underline{F}_{ij}^{n,(\tau-\Delta\tau)} + K_u^n \underline{\Delta S}^n,\ K_l^n \underline{S}^{n,(\tau)} x 10^{-3}\right) & if\ \Delta S^n < 0 \end{cases} \tag{18}$$

$$\underline{\Delta S}^n = \underline{S}^{n,(\tau)} - \underline{S}^{n,(\tau-\Delta\tau)} \tag{19}$$

where $\underline{F}_{ij}^{n,(\tau)}$ and $\underline{F}_{ij}^{n,(\tau-\Delta\tau)}$ denote the normal contact forces at time (τ) and (τ-$\Delta\tau$), respectively and $\underline{\Delta S}^n$ is the variation in overlap during the time step $\Delta\tau$. The factor 10^{-3} in Eq. (18) ensures that the force diminishes to zero as the overlap approaches zero.

The stiffness values during loading and unloading in Eq. (18) are calculated as follows:

$$\frac{1}{K_l^n} = \frac{1}{K_{li}^n} + \frac{1}{K_{lj}^n} \rightarrow K_l^n = \frac{K_{li}^n K_{lj}^n}{K_{li}^n + K_{lj}^n} \tag{20}$$

$$K_{li}^n = E_i d_p \tag{21}$$

where E_i represents the Young's modulus of the particle material, and d_p=2R_p is the particle size. Using this approach, the restitution coefficient ε related to the dissipated energy shown in Fig. 3, is given by:

$$\varepsilon^2 = \frac{K_l^n}{K_u^n} \tag{22}$$

Additionally, the DEM method accounts for tangential forces (denoted by the "t" superscript), which arise from friction. The software employs a linear elastic-frictional model [32-34]. Here, the tangential force calculation depends on whether sliding occurs. This can be expressed compactly as:

$$\underline{F}_{ij}^{t,(\tau)} = \min\left(\underline{F}_{ij}^{t,(\tau-\Delta\tau)} + K_l^n \underline{\Delta S}^t,\ \mu \underline{F}_{ij}^{n,(\tau)}\right) \tag{23}$$

where $\underline{F}_{ij}^{t,(\tau)}$ and $\underline{F}_{ij}^{t,(\tau-\Delta\tau)}$ are the tangential contact forces at times (τ) and (τ-$\Delta\tau$), respectively, $\underline{\Delta S}^t$ is the change in tangential overlap during the timeframe Δτ. The friction coefficient μ takes different values based on whether sliding occurs.

$$\mu = \begin{cases} \mu_s & if\ no\ sliding\ (static\ coeffcient) \\ \mu_d & if\ sliding\ (dynamic\ coeffcient) \end{cases} \tag{24}$$

When the tangential force exceeds the threshold $\mu_s \underline{F}_{ij}^{n,(\tau)}$, sliding is triggered. If the force falls below this limit, the contact reverts to the non-sliding condition.

To summarize, in this Eulerian-Lagrangian methodology, the fluid phase is still modeled using the Navier-Stokes equations. The exchange of momentum between phases is still determined by summing the contributions from all particles within the corresponding computational grid cell as shown by Eq. (9). Similar to the DDPM method, the paths of the particles are governed by a Newtonian equations of motion, applied individually to each particle or group (Eq.(4)). However, unlike in the DDPM, where particle-particle and particle-wall interactions are handled through the KTGF, these interactions are instead accounted for using the aforementioned soft-sphere model. Leaving aside for a while the related mathematical details, from a purely physical point of view this implies that, while in the soft-sphere approach, collisions between particles take a measurable amount of time, with the KTGF collisions are treated as nearly instantaneous, thereby

aligning with the hard-sphere model [35]. Although this may be regarded as a significant difference, in practice, it has been proven to produce negligible changes in terms of emerging behaviors in all those cases where the particle interaction times are much smaller than the characteristic temporal scale of the considered phenomena.

As concluding remark for this section, we wish to highlight that, by analogy with the DDPM approach, the DEM strategy also requires modification of the equations governing the fluid phase [33]. A physical interpretation is invoked by which the particles are seen as a porous medium with the porosity distribution being a function of the concentration of the solid phase as the simulation progresses. Accordingly the momentum balance equations for the fluid phase is recast as

$$\rho\frac{\partial(\phi\underline{V})}{\partial t}=-\phi\underline{\nabla}p-\rho\underline{\nabla}\cdot\left[\phi\underline{V}\underline{V}\right]+\underline{\nabla}\cdot\left[\mu\phi(\underline{\nabla V}+\underline{\nabla V}^{T})\right]$$
$$+\rho\phi b\ \omega^2\sin(\omega\ t)\underline{\hat{n}}+\underline{S}_m \tag{25}$$

where the fictious porosity ϕ is computed as

$$\phi = 1 - \varphi_p \tag{26}$$

where, as explained before, φ_p is the local particle volume fraction determined by using the instantaneous particle positions. In this way a balance equation for momentum similar to that used by the DDPM is recovered (see again eq. (13). For additional insights into this category of methods and related variants, the interested reader may consider [36-38].

3. Characteristic non-dimensional parameters

As is often the case, the complexity of the problem can be reduced by expressing it in terms of non-dimensional characteristic numbers. This approach significantly minimizes the number of variables that impact the system. They are the well-known Prandtl number (Pr=ν/α where ν is the fluid kinematic viscosity and α its thermal diffusivity) depending on the considered fluid, the nondimensional vibration frequency (Ω), the nondimensional acceleration amplitude (γ) and buoyancy factor (β) defined as:

$$\Omega=\frac{\omega L^2}{\alpha};\ \gamma=\frac{b\omega^2L^3}{\alpha^2};\ \text{and}\ \beta=(\beta_T\Delta T) \tag{27}$$

where β_T is the fluid thermal expansion coefficient. These parameters can be combined to form alternate characteristic numbers, namely, the classical (vibrational) Rayleigh number (Ra_ω)

$$Ra_\omega=\gamma\beta/\mathrm{Pr} \tag{28}$$

Other independent non-dimensional groups are the particle-to-fluid density ratio

$$\xi=\rho_P/\rho \tag{29}$$

the initial particle concentration (N_{part} total number of particles)

$$\Phi=\frac{N_{part}\frac{4}{3}\pi R_p^3}{L^3} \tag{30}$$

and the particle Stokes number

$$St=\frac{2}{9}\frac{R_p^2}{L^2} \tag{31}$$

for the sake of completeness it should also be noted that the alternate well-known definition of the Stokes number St_ξ, accounting for particle size and mass effect at the same time, may be recovered by multiplying St by ξ, i.e. $St_\xi=\xi St$).

While the above characteristic numbers are used to define the "case of interest", i.e. their specific values, taken together, define the "input" to be set for the numerical simulations, the related outcomes can be synthetically characterized by using another global parameter, namely, the so-called accumulation measure [39] defined as:

$$K(t)=\frac{1}{2(N_{part}-\tilde{n})}\sum_{i=1}^{N_{cell}}\left|k_i-\tilde{n}\right| \tag{32}$$

where N_{cell} is the total number of computational cells, $\tilde{n}$ is the average number of particle in each cell (N_{part} / N_{cell}) and k_i is the effective number of particles in the generic cell i. This parameter can be therefore be regarded as the normalized sum over the entire computational domain of the deviations of the number of particles $k_i(t)$ in each cell from the related average number. As such, it accounts for the degree of accumulation of particles, its limiting values 0 and 1 corresponding to particles evenly distributed in the domain and all concentrated in a single computational cell, respectively.

4. Results

Numerical simulations have been performed using the appropriate kernels (based on the models described in Sect. 3) of various computational platforms, namely, the one-way coupled, two-way coupled and the DDPM solvers of Ansys Fluent and the CFD-DEM numerical framework resulting from the combined exploitation of Ansys Fluent and the Rocky software for granular flows.

To properly mimic the space experiments, particles with three distinct density ratios have been considered for the computations, i.e. $\xi = 1.65,\ 0.177$ *and* 3.49, respectively, with the Stokes number being fixed to 3.1×10^{-6}. The host fluid is ethanol (Pr=18).

Before starting to deal with the outcomes of the analysis, for the convenience of the reader, we wish to recall here that, in general, in the absence of particles, the fluid flow generated by the application of vibrations to a differentially heated cubic cavity in a direction perpendicular to the imposed temperature gradient simply consists of a single roll occupying the entire transverse section of the cavity (the plane containing the vibrations and the temperature gradient), which periodically changes its circulation sense according to the forcing. In simple words, if the roll is oriented in the counterclockwise direction during the first half-cycle of vibrations, then it is oriented in the opposite (clockwise) direction during the second half-cycle as schematically shown in Fig. 4.

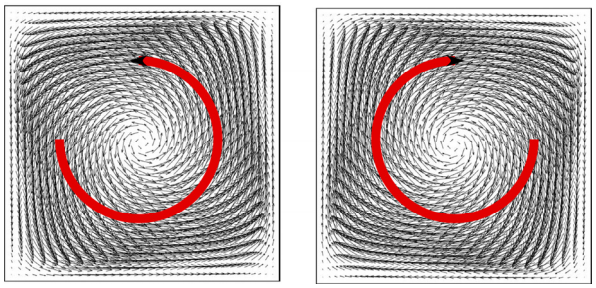

Fig. 4 – Sketch of convective flow developing in a cubic enclosure under the effect of vibrations and a temperature gradient perpendicular to the shaking direction at two distinct times evenly space within the vibration period.

The mechanism leading to recognizable structures when particles are added to the fluid has been described by Lappa [2]. It involves the concurrent action of three distinct influential factors, namely, purely inertial effects, by which (taken together) particles behave as a "compressible medium" (as they are not forced to follow the streamlines of the carrier incompressible fluid flow), convective effects, by which particles are transported in the liquid due to its viscous nature and confinement effects (i.e. under the effect of the body force induced by vibrations particles periodically hit the lateral boundaries of the cavity).

In this section, results are presented for only 3 of the 160 experiments that were conducted in space. This stems from a precise rationale. As already explained in the introduction, the main objective of this work is a critical discussion of the proper numerical approaches to be used in the attempt to capture properly the physics at play in the experiments rather than an exhaustive description and interpretation of them (which will be presented elsewhere). The simulations have been conducted by using a 40^3 mesh for the Eulerian equations and a given number of particles (as specified in the figure captions).

4.1 Run21 (heavy particles)

The outcomes of the numerical simulations for Run 21 ($\gamma=1.72\times10^{9}$, $Ra_{\omega}=4.81\times10^{5}$, $\Omega=1.667\times10^{4}$, $\xi=1.65$) are shown in Fig. 5. The classical two particle structures seen in the experiments can be clearly recognized in some panels of this figure.

In particular, the results are shown for an increasing level of complexity of the used numerical strategy. This is instrumental in showing that a varying degree of success is obtained according to the approach. As an example, while Fig. 5a reveals that the one-way coupled approach is successful in predicting the existence of specific loci where particles tend to be attracted as time passes (i.e. it can mimic to a certain extent the physics underlying the existence of the attractors), however, it also makes evident that the particle structures emerge with a shape much more regular and spatially extended than that effectively displayed by the experiments.

On the other hand, a close comparison of panels 5b, 5d and 5e, indicates that, although no morphological change occurs when passing from the standard two-way approach to the DDPM and finally to the CFD-DEM, more compact structures are obtained, especially when the outcomes of the DDPM simulation are considered (the transverse size of the two bands formed by particles on the left and right sides of the cavity attains a minimum in Fig. 5c).

Additional insights into the role played by the numerical model in determining the particle accumulation can be gathered from Fig. 6 where the aforementioned accumulation measure defined by eq. (32) has been plotted as a function of time. As quantitatively substantiated by the various curves, the accumulation process seems to be slightly faster when the DDPM model is used, which is consistent with what can be seen in Fig. 5.

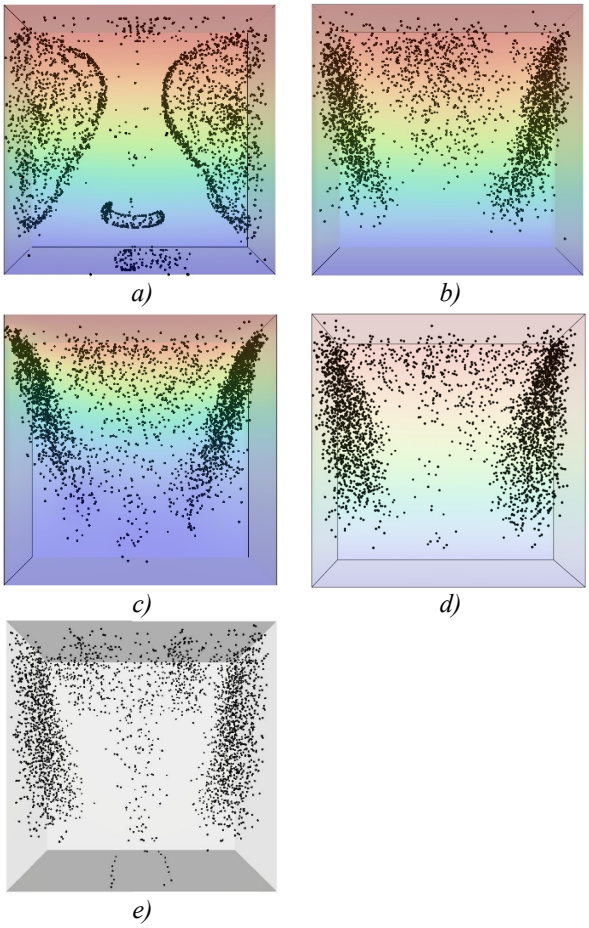

Fig. 5 - *Snapshot (perspective perpendicular to the yz mid-plane for t≅1300s) of particle structures and related temperature distribution for* $\gamma=1.72\times10^{9}$, $Ra_{\omega}=4.81\times10^{5}$, $\Omega=1.667\times10^{4}$, $\xi=1.65$ *and* $N_{part}=3150$: *a) one-way coupling, b) two-way coupling (DPM), c) DDPM without granular temperature PDE, d) DDPM with granular temperature PDE, e) CFD-DEM*

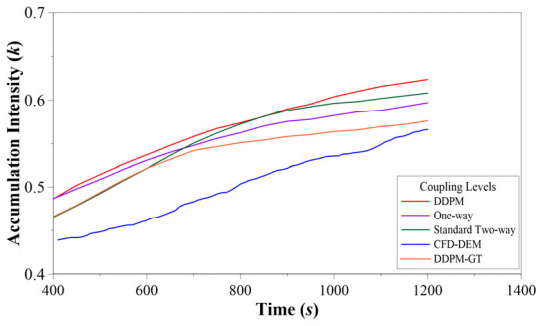

Fig. 6 - *Accumulation Intensity (K) as a function of time (t) for the same conditions considered in Fig. 5.*

In a quite unexpected way, however, the curve obtained with the CFD-DEM model lies under the corresponding curves obtained with the other models, which may indicate a lack of resolution in the related computations (we will return to this crucial aspect later).

4.2 Run33 (Light particles)

Following the same approach undertaken in the preceding section, here, we concentrate on the case where the particles have a density smaller than the carrier liquid ($\xi=0.177$) and assess critically the varying degree of success displayed by the different approaches described in Sect. 3 in capturing the physics.

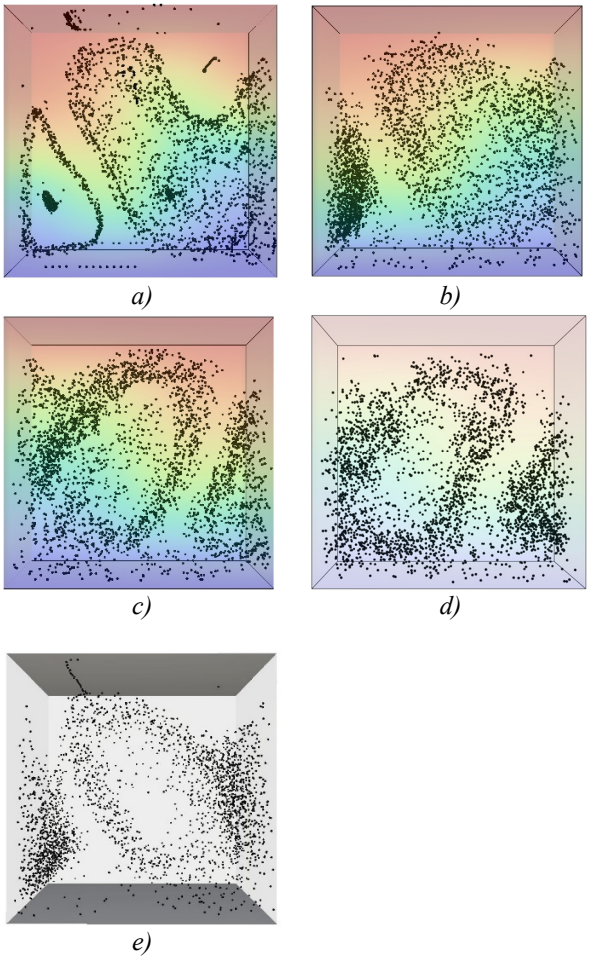

Fig. 7 - *Snapshots (perspective views perpendicular to the yz mid-plane for t≅1300s) of particle structures and related temperature distribution for* $\gamma=1.69\times10^{9}$, $Ra_{\omega}=1.77\times10^{6}$, $\Omega=2.33\times10^{4}$, $\xi=0.177$ *and* $N_{part}=3150$: *a) one-way coupling, b) two-way coupling (DPM), c) DDPM without granular temperature PDE, d) DDPM with granular temperature PDE, e) CFD-DEM.*

In this specific case, most surprisingly, four independent (physically disjoint) particle formations were observed during the experiments in certain ranges of the vibrational Rayleigh number (e.g., Run 33 for $\gamma=1.69\times10^{9}$, $Ra_{\omega}=1.77\times10^{6}$, and $\Omega=2.33\times10^{4}$). The corresponding numerical results are summarized in Fig. 7.

This case represents another valuable test case for different numerical strategies, given the unexpected increased multiplicity of particle structures (four formations in place of the classical two structures seen in other experiments).

Along these lines, panel 7a is instructive as, although it does not reproduce properly the experiments, it reveals the presence of a time-averaged flow breaking the symmetry of the emerging structures (the accumulation on the right side having a much larger spatial extension).

This non-zero-amplitude flow superimposed on the background oscillatory flow of thermovibrational nature is typically produced when the so-called Gershuni number defined as

$$Gs=\frac{(b\omega\beta_T\Delta TL)^2}{2\nu\alpha}=\frac{1}{2\,\mathrm{Pr}}\left(\frac{\beta\gamma}{\Omega}\right)^2=\frac{\mathrm{Pr}}{2}\left(\frac{Ra_{\omega}}{\Omega}\right)^2 \qquad (33)$$

takes relatively high values [5]. In this case its value is $Gs\cong5.1\text{x}10^{4}$ as opposed to the value $7.5\text{x}10^{3}$ related to Fig. 5, which explains why in this case a significant background "time-averaged" flow superimposed on the oscillating roll sketched in Fig. 4 exists.

When the back influence of particles on fluid flow is taken into account (Fig. 7b), a compactification of the small structure located on the left side can be seen. This is also a feature of the pattern shown in Fig. 7d (DDPM with granular temperature PDE) and 7e (CFD-DEM).

Surprisingly, none of the tested numerical approaches could successfully reproduce the experiments, which would require additional investigation. A possible root cause to explain this discrepancy might be sought in a departure of the effective thermal boundary conditions from the idealized ones used for the numerical simulations (a perfectly adiabatic behavior being assumed for the non-thermally active walls of the cubic cavity) or perhaps in the nature of the time-averaged flow itself, which might become time-dependent and oscillate in time with a frequency that does not match that of the imposed vibrations.

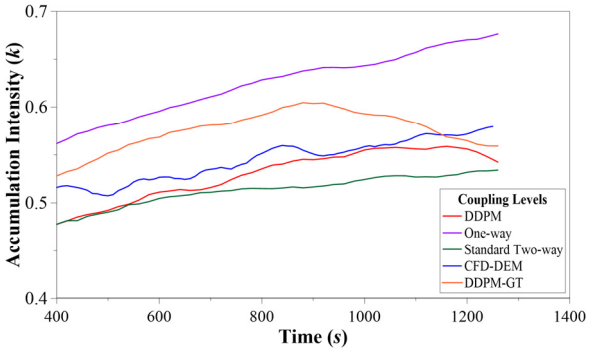

Fig.8. *Accumulation Intensity (K) as a function of time (t) for the same conditions considered in Fig. 7.*

In terms of formation time, Fig. 8 complements Fig.6 by showing that the formation time is apparently minimized when the one-way coupled solver is used, which however should be regarded as a non-physical effect given the insufficient level of fluid-particle coupling provided by this approach. The other three solvers provide comparable (similar) estimates.

4.3 Run29 (Extra Heavy Particles)

As a final case, we consider extra heavy particles, i.e. particles with a density exceeding by more than 3 times that of the host liquid (ξ=3.5). In this case, a single structure was revealed by the space experiment, which, given the absence of time-averaged flow ($Gs\cong1.5\text{x}10^{3}$ for this case for which $\gamma=1.09\times10^{9}$, $Ra_{\omega}=3.04\times10^{5}$, $\Omega=2.33\times10^{4}$), should be ascribed to a symmetry breaking instability driven by inertial effects (namely the back transfer of momentum from the particles to the fluid flow [8]).

Close inspection of Fig. 9, where all the numerical results have been summarized, immediately provides some important insights into the ability of the different approaches to capture the relevant "physics".

At a fixed time ($t\cong1300$ s), unlike all the other solvers, by which aggregates have already been formed, as witnessed by Fig. 9a, with the one-way coupling approach, the particle pattern is still in a transient stage of evolution (the two classical structures have not been completely formed yet). By contrast, these have already been formed when the two-way coupling model is used (Fig. 9b). None of these two methods, however, is able to capture the "single" structure revealed by the experiments at t = 1300 s.

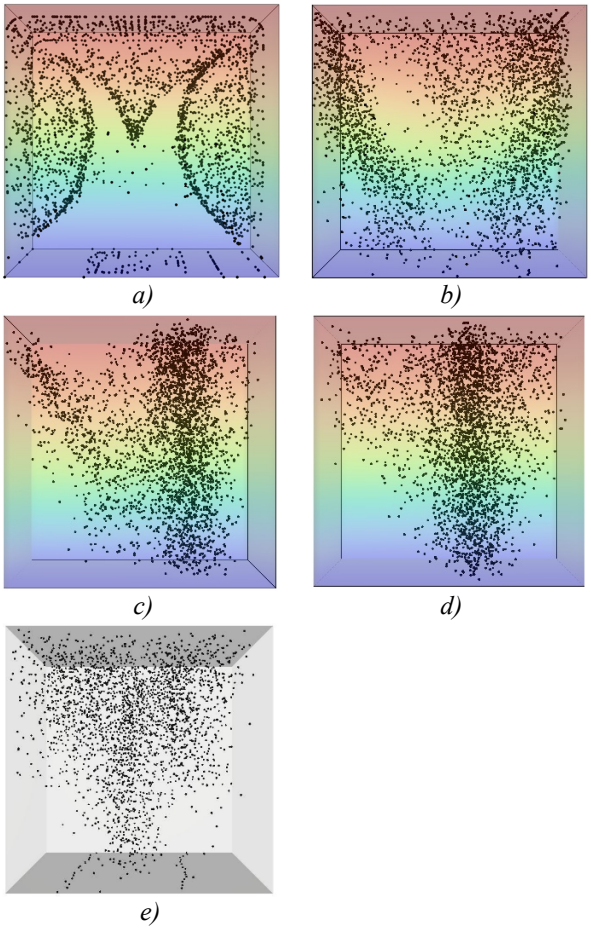

Fig.9. *Snapshots (perspective views perpendicular to the yz mid-plane for t≅1300s) of particle structures and related temperature distribution for* $\gamma=1.72\times10^{9}$, $Ra_{\omega}=4.81\times10^{5}$, $\Omega=1.667\times10^{4}$, $\xi=1.65$ *and* $N_{part}=3150$: *a) one-way coupling, b) two-way coupling (DPM), c) DDPM without granular temperature PDE, d) DDPM with granular temperature PDE, e) CFD-DEM.*

The outcomes of the DDPM simulation are shown in panels (c) and (d), which differ by a subtle aspect, i.e. the KTFG being switched off (Fig. 9c) and on (Fig. 9d), respectively. What stands immediately out from these two panels is that, in both cases a single formation is obtained after 1300 s. Moreover, cross comparison of the two-panels indicates that enabling the inter-particle stresses can help speed up this process, i.e. the transition from an initial configuration with two distinct accumulation regions to a single structure. A similar result is obtained when the CFD-DEM is used (where inter-particle stresses are an inherent feature of the model, and, as explained in Sect. 3, particle interactions are accounted for in the frame of a binary collision model reiterated over the entire population of particles).

The observations detailed above are corroborated by the measure of accumulation plotted in Fig. 10 where the one-way coupling curve clearly under-estimate the predictions of all the other models.

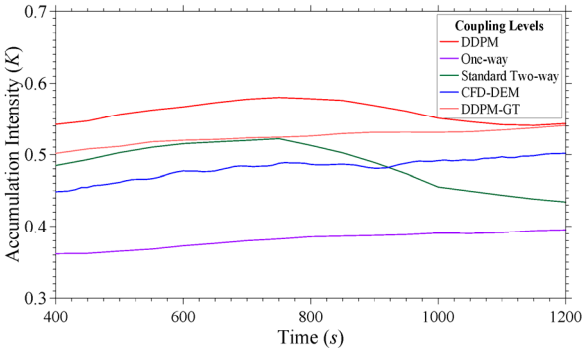

Fig.10. *Accumulation Intensity (K) as a function of time (t) for* $\gamma=1.72\times10^{9}$, $Ra_{\omega}=4.81\times10^{5}$, $\Omega=1.667\times10^{4}$, $St=3.1\times10^{-6}$ *and* $\xi=1.65$.

Figure 11 complements such results by showing in detail the transition from two to a single structure as predicted by the two-way coupling and the DDPM-KTFG solvers. The significance of this additional figure resides in its ability to make evident that the DDPM model captures the symmetry breaking at a slightly earlier stage and the particle accumulation density is restored to its former value and increases further compared to the standard two-way (DPM) model (by which the loss of magnitude of K fails to recover as the simulation progresses to the later stages).

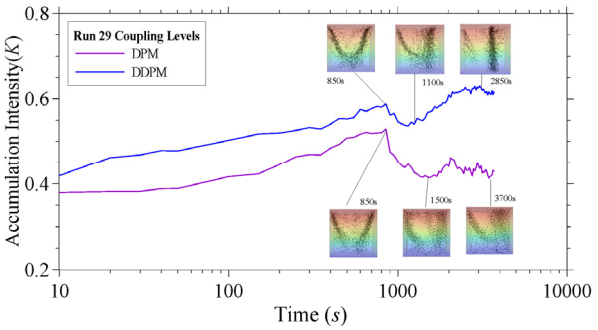

Fig.11 - *Accumulation intensity (K) as a function of time (t) in the logarithmic scale for* $\gamma=1.72\times10^{9}$, $Ra_{\omega}=4.81\times10^{5}$, $\Omega=1.667\times10^{4}$, $St=3.1\times10^{-6}$ *and* $\xi=1.65$ *depicting the symmetry breaking phenomena found in Run 29.*

6. Conclusions

This numerical study brings together 4 different numerical models potentially applicable to reproduce the outcomes of the T-PAOLA (PARTICLE VIBRATION) space experiment and get additional insights into the underpinning mechanisms.

The used approaches have displayed a varying degree of success in capturing the dynamics of interest, with outcomes that can be summarized as follows

While the one-way coupling model generally fails in predicting the effective morphology of structures revealed by the space experiments, this is properly captured by the two-way approach, which indicates that the back influence of the particles on the carrier flow plays a crucial role in shaping the emerging structures. In most cases the agreement becomes even better if the DDPM is exploited as the formations display a compactification in the transverse direction (the bands where particles accumulate become thinner). Accounting for the particle inter-stresses by means of the KTFG strategy has also another beneficial effect. It improves the ability of the numerical simulation to predict the inertial effects responsible for the transition from two initial distinct formations to a single structure.

Some counterintuitive results have been obtained in terms of CFD-DEM. Although in most cases, it provides patterns that are in good agreement with those obtained with the DDPM, it over-estimates or under-estimates the formation time depending on the considered case. This drawback may indicate an insufficient numerical resolution, i.e. a resolution not adequate to guarantee proper coupling of the Ansys Fluent Eulerian solver and the Lagrangian DEM solver implemented in Rocky.

Additional effort is therefore required to properly tune such a resolution and ensure consistency between the DDPM and CFD-DEM.

Acknowledgements

This work has been supported by the UK Space Agency (STFC grants ST/S006354/1, ST/V005588/1, ST/W002256/1 and ST/W007185/1) in the framework of the PARTICLE VIBRATION (T-PAOLA) project.

We also acknowledge the *ARCHIE-WeSt* High-Performance Computer (www.archie-west.ac.uk), which was used to produce some of the numerical results reported in this paper.

References

[1] Lappa M. (2024), "New In-Orbit Self-assembly principles and Manufacturing techniques", article in "Why Space? The Opportunity for Material Science and Innovation", a publication of UKRI-STFC and the Satellite Applications Catapult, https://sa.catapult.org.uk/why-space-the-opportunity-for-material-science-and-innovation/

[2] Lappa M., (2014), The patterning behaviour and accumulation of spherical particles in a vibrated non-isothermal liquid, Physics of Fluids (ISSN: 1070-6631), 26(9), 093301 (22 pages).

[3] Lappa M., (2017), On the multiplicity and symmetry of particle attractors in confined non-isothermal fluids subjected to inclined vibrations, Int. J. Multiphase Flow (ISSN: 0301-9322), 93: 71-83, https://doi.org/10.1016/j.ijmultiphaseflow.2017.03.015

[4] Lappa M., (2019), On the formation and morphology of coherent particulate structures in non-isothermal enclosures subjected to rotating g-jitters, Physics of Fluids (ISSN: 1070-6631), 31(7), 073303 (11 pages). https://doi.org/10.1063/1.5098438

[5] Lappa M. and Burel T., (2020), Symmetry Breaking Phenomena in Thermovibrationally Driven Particle Accumulation Structures, Physics of Fluids (ISSN: 1070-6631), 32(5), 053314 (23 pages), https://doi.org/10.1063/5.0007472

[6] Crewdson G., Evans M., Lappa M., (2022), Two-dimensional vibrationally-driven solid particle structures in non-uniformly heated fluid containers, Chaos (ISSN 1054-1500), 32(10) 103119 (13 pages). https://doi.org/10.1063/5.0104680

[7] Crewdson G. and Lappa M., (2022), An investigation into the behavior of non-isodense particles in chaotic thermovibrational flow, Fluid Dynamics & Materials Processing (ISSN: 1555-256X), 18(3), 497-510, https://doi.org/10.32604/fdmp.2022.020248

[8] Lappa M., (2022), Characterization of two-way coupled thermovibrationally driven particle attractee, Physics of Fluids (ISSN: 1070-6631), 34(5), 053109 (27 pages), https://doi.org/10.1063/5.0091520

[9] Lappa M. and Kao A., "Considerations for Material Properties & Processes in space & their impact", Chapter in "Why Space? The Opportunity for Material Science and Innovation", a publication of UKRI-STFC and the Satellite Applications Catapult, https://sa.catapult.org.uk/why-space-the-opportunity-for-material-science-and-innovation/

[10] Ratke L., Korekt G. and Drees S., (1998), "Phase separation and solidification of immiscible metallic alloys under low gravity", Adv. Space Res., 22(8), 1227-1236. https://doi.org/10.1016/S0273-1177(98)00152-5

[11] Lappa M., (2005) "Assessment of VOF Strategies for the analysis of Marangoni Migration, Collisional Coagulation of Droplets and Thermal wake effects in Metal Alloys under Microgravity conditions", Computers, Materials & Continua CMC (ISSN: 1546-2218), 2(1), 51-64.. https://doi.org/10.3970/cmc.2005.002.051

[12] Lappa M., Piccolo C., Carotenuto L., (2003), "Numerical and experimental analysis of periodic patterns and sedimentation of lysozyme", J. Cryst.

Growth (ISSN: 0022-0248), 254/3-4: 469-486.https://doi.org/10.1016/S0022-0248(03)01188-6

[13] Lappa M., Castagnolo D. (2003), "Complex dynamics of rhythmic patterns and sedimentation of organic crystals: a new numerical approach", Num. Heat Transfer Part B - Fundamentals (ISSN: 1040-7790), 43 (4): 373-401. https://doi.org/10.1080/713836224

[14] Lappa M., (2004),"Fluids, Materials and Microgravity: Numerical Techniques and Insights into the Physics", 538 pages, Elsevier Science (2004, Oxford, England).

[15] Shevtsova V., Lyubimova T., Saghir Z. et al., (2011), "IVIDIL: on-board g-jitters and diffusion controlled phenomena", J. Phys. Conf. Ser. 327(1), 012031.

[16] Shevtsova V., Mialdun A., Melnikov D., Ryzhkov I., Gaponenko Y., Saghir Z., Lyubimova T., "The IVIDIL experiment onboard the ISS: Thermodiffusion in the presence of controlled vibrations", Comptes Rendus Mécanique, 339 (5), 310-317, (2011)

[17] Santhosh B.M.and Lappa M., (2023), "On the relationship between solid particle attractors and thermal inhomogeneities in vibrationally-driven fluid-particle systems", Physics of Fluids (ISSN: 1070-6631), 35(10), 103316 (26 pages), https://doi.org/10.1063/5.0170162

[R18] Lappa M., Burel T., Kerr M., Crewdson G., Boaro A., Capobianchi P., Bonnieu S. V., Murphy L., Randall P., Hens S., (2022), Particle Vibration, an instrument to study particle accumulation structures on board the International Space Station, Microgravity Science & Technology (ISSN: 0938-0108), 34(3), article number 33 (24 pages).

[19] Maxey M. R. and Riley J. J., (1983), Equation of motion for a small rigid sphere in a nonuniform flow, Phys. Fluids, 26, 883-889.

[20 Lappa M., (2013), On the variety of particle accumulation structures under the effect of gjitters, J. Fluid Mech., 726, 160-195.

[21] Eaton J.K., (2009), Two-way coupled turbulence simulations of gas-particle flows using point-particle tracking, International Journal of Multiphase Flow 35, 792–800.

[22] Bianco V., Chiacchio F., Manca O., Nardini S., (2009), Numerical investigation of nanofluids forced convection in circular tubes, Applied Thermal Engineering, 29(17–18), 3632-3642.

[23] Adnan M., Sun J., Ahmad N. and Wei J.J. (2021), Comparative CFD modeling of a bubbling bed using a Eulerian–Eulerian two-fluid model (TFM) and a Eulerian-Lagrangian dense discrete phase model (DDPM), Powder Technology 383, 418–442.

[24] Cloete S., Amini S. and Johansen S.T., (2012), Performance evaluation of a complete Lagrangian KTGF approach for dilute granular flow modeling, Powder Technology, 226, 43-52.

[25] Lun, C. K. K., S. B. Savage, et al. (1984). "Kinetic Theories for Granular Flow: Inelastic Particles in Couette Flow and Slightly Inelastic Particles in a General Flow Field." Journal of Fluid Mechanics 140: 223-256.

[26] Gidaspow D, Bezburuah R, Ding J. Hydrodynamics of Circulating Fluidized Beds, Kinetic Theory Approach. 7th Engineering Foundation Conference on Fluidization 1992:75-82. https://www.osti.gov/biblio/5896246

[27] Richardson, D.C., Walsh, K.J., Murdoch, N. and Michel, P., (2011), Numerical simulations of granular dynamics: I. Hard-sphere discrete element method and tests. Icarus, 212(1), pp.427-437.

[28] Cundall, P.A., Strack, O.D.L., 1979. A discrete numerical model for granular assemblies. Géotechnique 29, 47–65.

[29] Schwartz, S.R., Richardson, D.C. and Michel, P., (2012), An implementation of the soft-sphere discrete element method in a high-performance parallel gravity tree-code. Granular Matter, 14, 363-380.

[30] Walton O.R., Braun R.L., (1986), Viscosity, granular-temperature, and stress calculations for shearing assemblies of inelastic, frictional disks, *J Rheol* (NY), 30, 949–980. https:// doi. org/ 10. 1122/1.549893

[31] Walton, O.R., (1993), Numerical simulation of inelastic, frictional particle-particle interactions. Particulate two-phase flow, 25, 884-911.

[32] Fonte C.B., Oliveira, Jr A.A.O., Almeida L.C. De (2015), DEM-CFD coupling : mathematical modelling and case studies using Rocky-Dem ® and Ansys Fluent ®. In: Eleventh international conference on CFD in the minerals and process industries. CSIRO Organization, Melbourne, Australia, pp 1–7

[33] Vivacqua V., López A., Hammond R. et al (2019) DEM analysis of the effect of particle shape, cohesion and strain rate on powder rheometry. Powder Technol 342: 653–663.

[34] Ansys-Rocky DEM Technical Manual, 2023, version R2.

[35] Ostermeier, P., DeYoung, S., Vandersickel, A., Gleis, S., & Spliethoff, H. (2019). Comprehensive investigation and comparison of TFM, DenseDPM and CFD-DEM for dense fluidized beds. Chemical Engineering Science, 196, 291-309.

[36] Tsuji, Y., Kawaguchi, T., and Tanaka, T. (1993). Discrete particle simulation of two-dimensional fluidized bed. Powder Technology, 77:79–87

[37] Hoomans, B., Kuipers, J., Briels, W., and Van Swaaij, W. (1996). Discrete particle simulation of bubble and slug formation in a two-dimensional gas fluidised bed: a hard-sphere approach. Chemical Engineering Science, 51:99–118.

[38] Lichtenegger, T., Pirker, S., 2018. CFD-DEM modeling of strongly polydisperse particulate systems. Powder Technol. 325, 698–711.

[39] Gotoda M., Sano T., Kaneko T., and Ueno I., (2015), Evaluation of existence region and formation time of particle accumulation structure (PAS) in half-zone liquid bridge, Eur. Phys. J.: Spec. Top. 224, 299.